Clim Dyn (2014) 43:2569–2583
DOI 10.1007/s00382-014-2146-0

Summertime land–sea thermal contrast and atmospheric circulation over East Asia in a warming climate—Part II: Importance of CO_2-induced continental warming

Youichi Kamae · Masahiro Watanabe ·
Masahide Kimoto · Hideo Shiogama

Received: 11 June 2013 / Accepted: 15 April 2014 / Published online: 29 April 2014

Abstract In this the second of a two-part study, we examine the physical mechanisms responsible for the increasing contrast of the land–sea surface air temperature (SAT) in summertime over the Far East, as observed in recent decades and revealed in future climate projections obtained from a series of transient warming and sensitivity experiments conducted under the umbrella of the Coupled Model Intercomparison Project phase 5. On a global perspective, a strengthening of land–sea SAT contrast in the transient warming simulations of coupled atmosphere–ocean general circulation models is attributed to an increase in sea surface temperature (SST). However, in boreal summer, the strengthened contrast over the Far East is reproduced only by increasing atmospheric CO_2 concentration. In response to SST increase alone, the tropospheric warming over the interior of the mid- to high-latitude continents including Eurasia are weaker than those over the surrounding oceans, leading to a weakening of the land–sea SAT contrast over the Far East. Thus, the increasing contrast and associated change in atmospheric circulation over East Asia is explained by CO_2-induced continental warming. The degree of strengthening of the land–sea SAT contrast varies in different transient warming scenarios, but is reproduced through a combination of the CO_2-induced positive and SST-induced negative contributions to the land–sea contrast. These results imply that changes of climate patterns over the land–ocean boundary regions are sensitive to future scenarios of CO_2 concentration pathways including extreme cases.

Keywords Land–sea thermal contrast · East Asia · Global warming · CMIP5 · Radiative forcing

1 Introduction

Recent modeling studies have shown that the increase of surface air temperature (SAT) over land is larger than that over the ocean in global warming experiments (e.g. Manabe et al. 1991; Dommenget 2009; Dong et al. 2009; Boer 2011). This robust feature, namely the change in land–sea thermal contrast, has also been confirmed in the recent trend of observational data (e.g. Lambert and Chiang 2007; Sutton et al. 2007; Jones et al. 2013). The projected future change in land–sea SAT contrast could influence regional atmospheric circulations in a warming climate (e.g. Kamae et al. 2014, hereafter Part I).

The physical mechanisms for the increasing global land–sea SAT contrast in a warming climate have been investigated by using coupled atmosphere–ocean general circulation models (CGCMs) and atmosphere-only general circulation models (AGCMs) in previous studies (Lambert and Chiang 2007; Joshi et al. 2008; Dommenget 2009; Dong et al. 2009; Boer 2011; Lambert et al. 2011; Joshi et al. 2013). The land–sea contrast is strengthened in both transient and equilibrium responses to external forcing (Manabe et al. 1991). However, the increasing land–sea SAT contrast in a warming climate is not simply a

Y. Kamae (✉) · H. Shiogama
Center for Global Environmental Research, National Institute for Environmental Studies, 16-2 Onogawa, Tsukuba, Ibaraki 305-8506, Japan
e-mail: kamae.yoichi@nies.go.jp

M. Watanabe · M. Kimoto
Atmosphere and Ocean Research Institute, University of Tokyo, 5-1-5 Kashiwanoha, Kashiwa, Chiba 277-8568, Japan

H. Shiogama
Environmental Change Institute, University of Oxford, South Parks Road, Oxford OX1 3QY, UK

consequence of the different thermal inertias between land and ocean, but originates from the different properties of the surface and boundary layer between the land and ocean (Manabe et al. 1991; Sutton et al. 2007; Joshi et al. 2008; Dong et al. 2009). In response to ocean surface warming, enhanced evaporation results in a smaller SAT change compared with the land surface (Manabe et al. 1991; Sutton et al. 2007). Joshi et al. (2008) showed that temperature change in the lower free troposphere above the boundary layer (i.e. 600–700 hPa level) was similar over land and ocean and that the land–sea thermal contrast in a warming climate was confined to the boundary layer. They then suggested that the lapse rate change in the boundary layer over the ocean, in response to sea surface temperature (SST) increase, is larger than that over land because of the difference in relative humidity and the associated lapse rate between land and ocean (see Fig. 1 in Joshi et al. 2013). Compo and Sardeshmukh (2009) demonstrated that the bulk of the global-scale annual-mean land surface warming in recent decades could be largely reproduced by AGCM experiments forced by observed SST increase. In addition, stomatal closure in response to CO_2 increase and the associated decrease of cloud amount also affect the land–sea SAT contrast in future projections (e.g. Dong et al. 2009; Doutriaux-Boucher et al. 2009).

The change in the land–sea SAT contrast can influence atmospheric thermodynamic structures and associated circulation patterns in a warming climate (e.g. Ueda et al. 2006; Dong et al. 2009; Sun et al. 2010; Fasullo 2012; Li et al. 2012; Wu et al. 2012; Zhu et al. 2012; Bayr and Dommenget 2013). For example, the land–sea SAT contrast over the Far East in boreal summer has increased in recent decades (0.11 K decade^{-1}, Part I). This trend is expected to continue in future warming projection obtained from general circulation models (GCMs) conducted in Coupled Model Intercomparison Project phase 5 (CMIP5; Taylor et al. 2012). In the future climate projections, it was also revealed that the land SAT and geopotential height in the mid-troposphere over the Far East increase in a GCM accompanying anomalous pressure and atmospheric circulation patterns over East Asia. This manifests as a stronger surface anticyclone over the Okhotsk high area and around the Philippines, an increase of cold northeasterly wind over northern Japan called Yamase, and strengthened rainfall over the Meiyu–Baiu front (Kimoto 2005; Arai and Kimoto 2008; Part I).

Kimoto (2005) showed that the increase of CO_2 concentration in the atmosphere alone induces a continental warming and an associated summertime atmospheric circulation pattern over East Asia in an AGCM simulation (Fig. 4b in Kimoto 2005). In transient warming experiments conducted by CGCMs, the global-mean SAT (SAT_g) increases gradually with time, in response to the increase of CO_2 concentration in the atmosphere. However, the direct radiative effect of continuously increasing amounts of CO_2 and the effect of an increase of SST have played distinct roles in recent climate change (e.g. Folland et al. 1998; Bracco et al. 2004; Deser and Phillips 2009). The warming of the troposphere and land surface by CO_2 radiative forcing plays an important role in changes to the hydrological cycle and atmospheric circulations (e.g. Mitchell et al. 1987; Allen and Ingram 2002; Gregory and Webb 2008; Cao et al. 2012; Bony et al. 2013; Chadwick et al. 2014), cloud, and radiation (e.g. Gregory and Webb 2008; Kamae and Watanabe 2012, 2013; Tomassini et al. 2013) in a warming climate. Kamae and Watanabe (2013) revealed the changes in cloud, precipitation, and atmospheric circulation through the change in land–sea SAT contrast in the fast response to the atmospheric CO_2 quadrupling. However, the seasonal and regional responses in the atmospheric circulation, their mechanisms, and their consistency among different GCMs have not been examined sufficiently. In this paper, we investigate the possible roles of the SST effect and CO_2 direct radiative effect on projected future changes over the Far East during boreal summer (Part I) and their consistencies by using the CMIP5 multi-model dataset. In CMIP5, we can investigate the roles of CO_2 and SST by using sensitivity experiments prescribing the CO_2 concentration and SST with multi-AGCMs. We also attempt to decompose the contributions of the two effects in idealized transient experiments and future scenario experiments by using a reconstruction method detailed below. Section 2 describes the model, experiments and methods. Section 3 presents the roles of CO_2 and SST on the changes in idealized simulations forced by the transient CO_2 increase. In Sect. 4, the roles of them in future scenario experiments are also examined. Section 5 presents a discussion and implication. Section 6 describes the conclusions of Parts I and II.

2 Data and methods

2.1 CMIP5 model ensemble and experiments

In this study, we used the CMIP5 multi-model dataset (Taylor et al. 2012) to analyze the results of idealized transient experiments, as in Part I. In Part II, the abrupt change in response to CO_2 quadrupling and the equilibrium responses in atmosphere-only model experiments are also investigated, in order to quantify the contributions of different forcings (see Sect. 2.2).

We used nine models for which all the outputs of transient and sensitivity runs required are available (Table 1). For the idealized transient experiments, a 1 %/year CO_2 increase experiment (hereafter 1 % CO_2) is used. In 1 % CO_2, the

Table 1 Changes in global-mean SAT (ΔSAT_g), land–sea SAT ($\Delta SAT_{lnd} - \Delta SAT_{ocn}$) and thickness contrasts ($\Delta Z3085_{lnd} - \Delta Z3085_{ocn}$) over the Far East (110°E–170°E, 30°N–70°N), and orthogonal wind speed at 150°E, 500 hPa level ($\Delta U_{orth}500_{150E}$) simulated in 1 % CO_2 run (CGCM) with CMIP5 nine models (similar to Table 1 in Part I)

	ΔSAT_g (K)			$\Delta SAT_{lnd} - \Delta SAT_{ocn}$ (K)			$\Delta Z3085_{lnd} - \Delta Z3085_{ocn}$ (m)			$\Delta U_{orth}500_{150E}$ (m s^{-1})		
	CGCM	CO_2	SST	CGCM	CO_2	SST	CGCM	CO_2	SST	CGCM	CO_2	SST
BCC-CSM1-1	3.54	0.49	4.64	1.08	1.96	−0.37	19.42	54.78	−23.61	−1.62	−1.87	1.54
CNRM-CM5	3.86	0.46	4.49	0.21	1.26	−0.84	−1.46	21.78	−20.22	−0.06	−0.02	0.33
CanAM4/CanESM2	4.56	0.51	4.68	1.76	1.43	−0.59	40.14	37.54	−28.14	−0.95	−0.98	0.34
HadGEM2-A/HadGEM2-ES	4.60	0.37	4.72	1.70	1.23	−0.06	22.21	29.22	−25.37	−1.12	−0.08	0.19
IPSL-CM5A-LR	4.34	0.45	4.19	0.95	0.94	−1.60	32.39	19.90	−6.07	−0.93	−0.33	−0.81
MIROC5	2.94	0.56	4.61	0.74	1.66	−0.69	24.05	39.11	−33.70	−1.11	−0.05	0.39
MPI-ESM-LR	4.14	0.46	4.61	1.31	1.20	−2.04	−2.17	13.11	−61.00	−0.67	−0.42	2.69
MPI-ESM-MR	4.01	0.44	4.48	1.22	1.27	−2.13	1.75	19.64	−60.51	−0.20	−0.61	2.99
MRI-CGCM3	3.20	0.38	4.52	−0.09	0.90	−1.06	−0.81	33.12	−34.48	0.24	−0.98	1.48
Ensemble	3.91 ± 0.56	0.46 ± 0.06	4.55 ± 0.15	0.99 ± 0.59	1.32 ± 0.31	−1.04 ± 0.69	15.06 ± 15.20	29.80 ± 12.14	−32.57 ± 17.00	−0.71 ± 0.57	−0.59 ± 0.57	1.02 ± 1.18

The anomalies are calculated by differences between the years 111–140 and the corresponding period in control run. $\Delta Z3085_{lnd} - \Delta Z3085_{ocn}$ is calculated by difference of thickness (between 300 and 850 hPa) averaged over 130°E–145°E and 146°E–160°E along the land-to-ocean line (130°E, 65°N–160°E, 35°N, Fig. 4a). CO_2 and SST rows represent changes in 30-year climatologies of amip4× CO_2 and amipFuture runs relative to amip run. The uncertainties for the ensemble mean of nine models are ±1 SDs

atmospheric CO_2 concentration is prescribed and increased by 1 %/year starting from 1850 of a pre-industrial control simulation until a quadrupling of the CO_2 concentration is achieved with respect to the pre-industrial levels after 140 years. All the other external forcings such as aerosols are kept at their pre-industrial values. Anomaly Δ of any variables in 1 % CO_2 run shown in this study is defined by the difference between averages over the last 30 years in 1 % CO_2 run (111–140) and corresponding 30 years in the pre-industrial control simulation. To quantify the possible contributions of atmospheric CO_2 and SST forcing on the results of the 1 % CO_2 run, we analyzed an Atmospheric Model Intercomparison Project (AMIP) type control (amip) and two sensitivity experiments; amip4 × CO_2 and amipFuture (Bony et al. 2011; Taylor et al. 2012). In amip and amip4 × CO_2, the models were driven by observation-based SST and sea–ice concentration for 1979–2008 with atmospheric CO_2 concentration set to 280 and 1,120 ppmv, respectively. In amipFuture, a spatially patterned SST increase, derived from a multi-model ensemble mean of the 1 % CO_2 experiment in CMIP phase 3, is superimposed on the observed SST prescribed in amip. In Sect. 3.1, we also analyzed amip4 K run in which spatially-uniform +4 K SST is superimposed on the SST to examine a sensitivity of results on the spatial pattern of the imposed SST. Global-mean anomaly of the SST in amipFuture is equal to that in amip4 K (i.e. 4 K). Anomaly Δ is defined by the difference of 30-year averages between sensitivity runs (amip4× CO_2, amip4 K, and amipFuture) and control run (amip). These sensitivity experiments were also utilized in the previous studies examining climate feedbacks (Webb and Lock 2013; Demoto et al. 2013), changes in the hydrological cycle (Bony et al. 2013; Huang et al. 2013; Ma and Xie 2013; Widlandky et al. 2013), and tropospheric and land adjustments to increasing CO_2 (Kamae and Watanabe 2012, 2013; Tomassini et al. 2013).

We also examined the results of historical (1850–2005) and future scenario (2006–2100) experiments; the latter forced by a representative concentration pathway (RCP) of future anthropogenic changes in atmospheric compositions, by using the MIROC5 model (Watanabe et al. 2010). The RCP runs have four types of scenarios (RCP2.6, RCP4.5, RCP6.0, and RCP8.5, Meinshausen et al. 2011). Δ in RCP runs are calculated by anomalies of 30-year averages (2041–2070 and 2071–2100) from 111-year average (1850–1960) in the historical simulation (Table 2). Furthermore, we investigated the rapid change due to abrupt CO_2 increase, and slow change associated with SAT_g increase, by using the abrupt4× CO_2 run (hereafter step experiment), which is branched off from the control run by instantaneously quadrupling the CO_2 concentration from its pre-industrial level and holding it fixed. Δ is calculated by anomaly from the corresponding mean state of the pre-industrial control simulation.

2.2 Reconstruction of idealized transient and future scenario runs with CO_2 step experiment

In the AMIP-type experiments, we can determine explicitly two factors for the changes in land–sea contrast: direct radiative forcing due to CO_2 increase (CO_2 effect) and surface warming (SST effect). As for the responses in the idealized transient experiments using CGCMs, the simulated changes in land–sea contrast are composed of the two factors. In Sect. 4, we attempt to decompose the two by using a method below.

First, we reconstruct the response y_i in the 1 % CO_2 with the step experiment at year i, by using a method proposed in Good et al. (2011, 2013):

$$y_i = \sum_{j=o}^{i} w_{i-j} x_j, \tag{1a}$$

$$w_{i-j} = \frac{\Delta F_{i-j}}{\Delta F_{4\times CO_2}}, \tag{1b}$$

where x_j is the response of the same variable at year j of the step experiment. w_{i-j} is a scaling factor of the annual-mean radiative forcing change from year i to year j of the given scenario (ΔF_{i-j}) relative to the radiative forcing due to CO_2 quadrupling ($\Delta F_{4\times CO_2}$). We obtained $\Delta F_{4\times CO_2} = 8.70$ W m^{-2} by the amip4× CO_2 experiment (Kamae and Watanabe 2013).

As for the RCP runs, we follow the method of Forster and Taylor (2006) to estimate w_{i-j} from the output of the model experiments [Eq. (2) in Good et al. 2013] to take into account the CO_2 and non-CO_2 forcings, such as aerosols and land use changes. The global-mean net radiative flux at the top of atmosphere (N, positive downward) is approximated by global-mean radiative forcing and ΔSAT_g as:

$$F = N + \lambda \Delta SAT_g, \tag{2}$$

where F is the radiative forcing and λ is the climate feedback parameter. We obtain $\lambda = 1.69$ W m^{-2} K^{-1} from the least-square regression coefficient of N to ΔSAT_g in the step experiment (Kamae and Watanabe 2013) by following the method of Gregory et al. (2004). Equation (2) can be used to estimate the time-varying F from the simulated time-series of N and ΔSAT_g. The applicability of this method to the Far East land–sea contrast is discussed in Sects. 4 and 5.

3 Distinct roles of CO_2 forcing and SST increase on the land–sea contrast

3.1 Global and regional changes

As a prelude, we reconfirm the spatial pattern of ΔSAT in global warming experiment shown in Part I. Figure 1a shows the June–August (JJA)-mean ΔSAT in the 1 % CO_2 run by the nine CMIP5 models. Similar to the earlier studies, positive ΔSAT is generally larger over land than over the ocean. An anomalous warming over the Arctic Ocean, the so-called arctic amplification (e.g. Serreze and Barry 2011), is not found during boreal summer (Fig. 1a). The maximum warming associated with decreasing sea ice cover occurs over the Barents Sea and Antarctic Ocean. In low latitudes, the warming is large in the eastern equatorial Pacific and western equatorial Indian Ocean associated with the spatial pattern of projected SST increase (e.g. Collins et al. 2010). Figure 1e shows the change in temperature (T) at the 700 hPa level (ΔT_{700}), representing the free tropospheric response. In contrast to ΔSAT, ΔT_{700} represents a zonally uniform increase independent on the distribution of land and ocean. The rest panels of Fig. 1 show the effects of CO_2 quadrupling, uniform and patterned SST +4 K identified in the AMIP-type sensitivity experiments (amip4× CO_2 minus amip, amip4 K minus amip and amipFuture minus amip, respectively). Consistent with earlier reports (Joshi et al. 2008; Compo and Sardeshmukh 2009), SST increase alone without radiative forcing could establish the land–sea ΔSAT contrast in low latitudes (Fig. 1c, d), whereas the land–sea ΔT_{700} contrast is not clearly found (Fig. 1g, h). In the amip4× CO_2 run, both ΔSAT and ΔT_{700} over land (ocean) increase (change little) owing to the CO_2-induced continental warming in contrast to the fixed ocean temperature (Fig. 1b, f). Note that the continental warming due to the CO_2 increase is also found in the other seasons (figure not shown).

Some differences are found in the responses between amip4 K and amipFuture. For example, the surface warming over the eastern equatorial Pacific and western equatorial Indian Ocean (over Southern Hemisphere mid- and high-latitude) are larger (smaller) in amipFuture relative to amip4 K associated with the spatial pattern of imposed SST anomaly in amipFuture (e.g. Fig. 1 in Lu et al. 2008). These differences are important for atmospheric circulations, regional moisture convergence, and precipitation responses in a warmer climate over the tropics and subtropics (Huang et al. 2013; Ma and Xie 2013; Widlandky et al. 2013). In contrast, the warming over land area (both at the surface and 700 hPa) over Northern Hemisphere mid- and high-latitude (40°N–80°N) both in amip4 K and amipFuture runs are relatively smaller than those over the ocean (Fig. 1c, d, g, h). These results indicate that the sign of change in the free-tropospheric (and surface) land–sea temperature contrast does not depend on whether the imposed SST is uniform or patterned. We only show the results derived from amipFuture run hereafter because the spatial pattern of the imposed SST in amipFuture is rather similar to that of SST anomaly simulated in 1 % CO_2 run than the uniform increase. Note that spatial

Table 2 Global-mean radiative forcing (ΔF), ΔSAT_g, and the land–sea contrasts over the Far East simulated in MIROC5

	ΔF (W m^{-2})	ΔSAT_g (K)	$\Delta SAT_{lnd} - \Delta SAT_{ocn}$ (K)	$\Delta Z3085_{lnd} - \Delta Z3085_{ocn}$ (m)	$\Delta U_{orth}500_{150E}$ (m s^{-1})
CGCM	7.84	2.94	0.74	24.05	−1.11
CO_2	8.70	0.56	1.66	39.11	−0.28
SST	0.00	4.61	−0.69	−33.70	0.34
RCP2.6					
2041–2070	3.44 ± 0.07	1.33 ± 0.04	−0.07 ± 0.05	2.46 ± 5.26	−0.30 ± 0.13
2071–2100	3.23 ± 0.06	1.33 ± 0.06	0.02 ± 0.04	4.75 ± 4.91	−0.31 ± 0.20
RCP4.5					
2041–2070	4.23 ± 0.05	1.58 ± 0.04	0.12 ± 0.04	4.86 ± 3.68	−0.24 ± 0.21
2071–2100	4.82 ± 0.08	1.90 ± 0.04	0.14 ± 0.07	4.50 ± 4.89	−0.12 ± 0.18
RCP6.0					
2041–2070	3.78	1.40	0.19	8.97	−0.65
2071–2100	5.60	2.11	0.19	14.49	−0.31
RCP8.5					
2041–2070	5.58 ± 0.05	2.07 ± 0.04	0.28 ± 0.10	5.93 ± 7.90	−0.09 ± 0.30
2071–2100	8.51 ± 0.05	3.26 ± 0.02	0.39 ± 0.10	16.72 ± 3.55	−0.82 ± 0.09
ΔF effect	8.70	–	2.06	26.52	−1.00
ΔSAT_g effect (K^{-1})	–	1.00	−0.39	−3.91	0.09

The anomalies of RCP runs are calculated by differences of 30-year climatologies (2041–2070 and 2071–2100) and 111-years (1850–1960) in the historical simulation. The values and the ranges of RCP2.6, 4.5, and 8.5 are three-member ensemble means and ±1 SDs. The ΔF and ΔSAT_g effects are determined by the y-axis intercept and slope of the regression line derived from step experiment detailed in Sect. 4

patterns of the SST anomaly simulated in 1 % CO_2 in CMIP5 models show some differences with the imposed SST pattern in amipFuture run (see Sects. 3.2, 5).

Figure 2 shows the zonally-averaged land- and ocean-mean ΔSAT during JJA in the 1 % CO_2, AMIP-type CO_2 quadrupling and patterned +4 K SST experiments. In amipFuture run, the land-mean ΔSAT is larger than the ocean-mean ΔSAT in low latitudes (35°S–40°N, Fig. 2c). Hence the established land–sea ΔSAT contrast is confined to low latitudes (35°S–40°N), which is inconsistent with the results of the 1 % CO_2 run. The ΔSAT contrast in mid- and high-latitudes in the Northern Hemisphere (40°N–70°N) found in the 1 % CO_2 run (Figs. 1a, 2a) exhibits in the experiment with CO_2 radiative forcing (Figs. 1b, 2b).

On a global perspective, previous studies have revealed that the spatially uniform warming in the free troposphere in response to SST increase induces land–sea ΔSAT contrast through the difference in lapse rate in the boundary layer between land and ocean (Joshi et al. 2008; Compo and Sardeshmukh 2009; Dommenget 2009). However, this mechanism does not work efficiently in mid- and high-latitudes in the Northern Hemisphere during boreal summer. Figure 3 shows the vertical profile of difference between land-mean ΔT and ocean-mean ΔT in response to patterned +4 K SST increase (amipFuture minus amip) in global-mean and the Far East (110°E–170°E, 30°N–70°N). On a global perspective (Joshi et al. 2008), ΔT_{700} over both land and ocean shows similar values, resulting in a land–sea temperature contrast in the boundary layer due to the difference of lapse-rate between the land and the ocean (Figs. 1d, h, 3). In contrast, the land-mean ΔT_{700} in response to patterned +4 K SST increase is smaller than that over the ocean in mid- and high-latitudes in the Northern Hemisphere including the Far East (Figs. 1d, h, 3). In the tropics, the free-tropospheric warming tends to be homogenized because of the large Rossby radius of deformation, often referred to as the weak temperature gradient (Sobel et al. 2001). However, free-tropospheric temperature over the continental interiors in mid- and high-latitude is less sensitive to the SST increase owing to the smaller Rossby radius of deformation than that in low latitude (Figs. 1g, h, 3). The smaller warming of free troposphere over land than ocean results in a negative or no land–sea ΔSAT contrast over mid- and high-latitude including the Far East (Figs. 1, 2, 3). The response of the warming contrast over East Asia to the uniform SST increase is similar to that to the patterned SST increase (Fig. 1c, d, g, h), indicating that the sign of the response of the land–sea contrast is not sensitive to whether the imposed SST is uniform or patterned.

3.2 Thermodynamic structure over the Far East

Given the essential component of the CO_2-induced continental warming for the land–sea ΔSAT contrast in the global warming projection, we focused on the thermodynamic

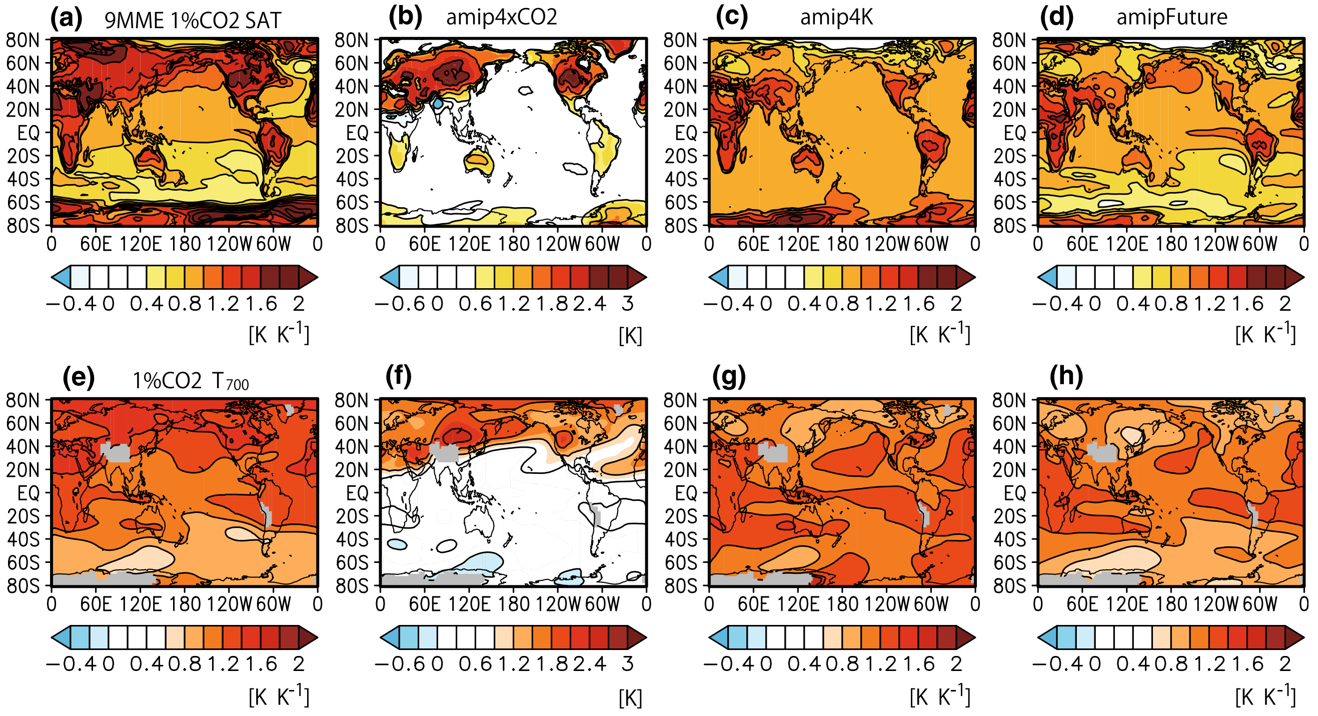

Fig. 1 CMIP5 nine models ensemble means of JJA-mean **a–d** Δ*SAT* (K) and **e–h** difference of temperature (Δ*T*) at 700 hPa (ΔT_{700}, K). Model means in **a**, **c**, **d**, **e**, **g**, **h** are calculated with normalized values (K^{-1}) by global-mean Δ*SAT* (ΔSAT_g) in the individual models. The anomalies are calculated by averages in 30 years of **a**, **e** 1 % CO_2 run (111–140) relative to control run, **b**, **f** amip4× CO_2, **c**, **g** amip4 K and **d**, **h** amipFuture run relative to amip run

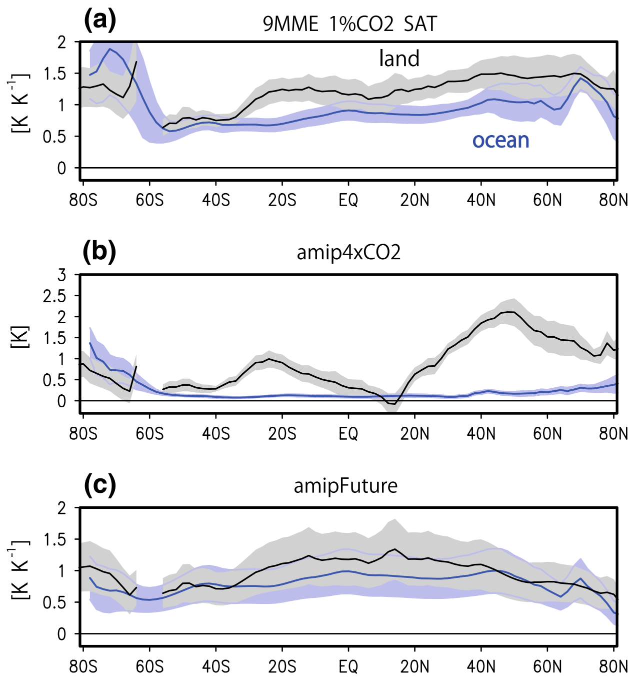

Fig. 2 Zonal-mean Δ*SAT* in JJA over land (*black*) and ocean (*blue*) in **a** 1 % CO_2 run relative to control run, **b** amip4× CO_2 and **c** amipFuture run relative to amip run. **a**, **c** Normalized by ΔSAT_g. Shadings represent ±1 SDs in nine models

structure in the troposphere over the Far East. We also examined changes in atmospheric circulation which is tightly associated with the change of the tropospheric thermodynamic structure over East Asia (Part I). Figures 4 and 5 compare the changes in thickness and geopotential height in the 1 % CO_2 and two AMIP sensitivity runs. The change in thickness between 300 and 850 hPa (Δ*Z3085*) can be used as an index of tropospheric temperature change. As shown in Part I, the tropospheric warming over the Eurasian continent induces an anticyclonic anomaly in the upper troposphere, the land–sea Δ*Z3085* contrast (Fig. 4a), and an associated change in the East Asian atmospheric circulation (Fig. 4; Table 1). Figure 4b, c show the effects of CO_2 quadrupling and patterned +4 K SST increase. Tropospheric warming over the ocean is larger than that over land in response to the SST increase (Fig. 4c). This result is consistent with the larger Δ*SAT* over the ocean than the land (Fig. 1d). The anomalous tropospheric warming over the ocean induces negative land–sea thermal and geopotential height contrasts in the upper troposphere (Figs. 4c, 5c and curve in Fig. 5f). In contrast, CO_2 quadrupling induces the anomalous tropospheric warming over the continent and associated positive contrasts (Figs. 4b, 5b, e), which is consistent with that simulated in the 1 % CO_2 run (Figs. 4a,

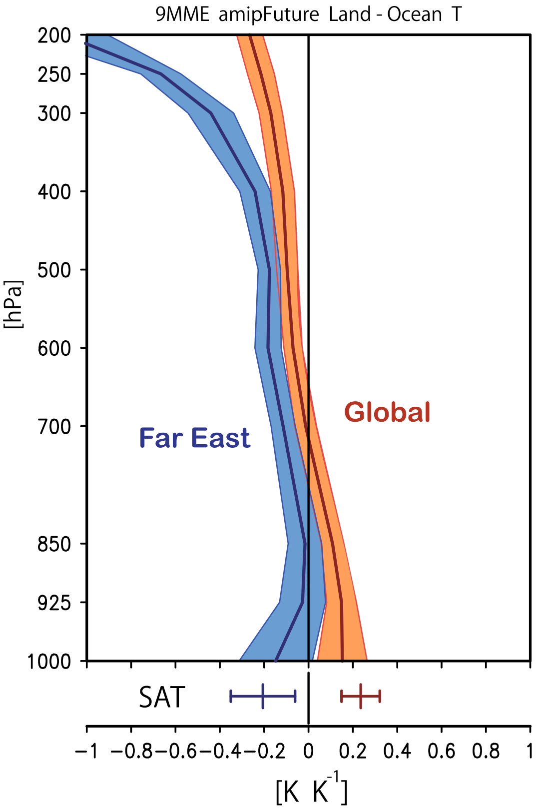

Fig. 3 Vertical profile of normalized global-mean (*orange*) and the Far East mean (*blue*) ΔT difference between land and ocean (K K^{-1}) in amipFuture run relative to amip run. *Solid curves* and *shadings* represent the nine models ensemble means and ±1 SDs. Crosses at bottom of the panel represent the normalized ΔSAT difference between land and ocean (K K^{-1})

5a, d). Note that the maximum warming in the upper troposphere, particularly over low latitude (Fig. 5a) is attributed to the SST increase (Fig. 5c). Spatial distribution of horizontal wind at 850 hPa level shows northeasterly anomaly over East Asia in 1 % CO$_2$ run (Fig. 4a, Part I). Figure 4 also shows that the spatial distributions of changes in the dynamical circulation are tightly coupled with the spatial patterns of tropospheric thermodynamic structure over East Asia in the three runs (1 % CO$_2$, amip4× CO$_2$, and amipFuture). An index of dynamical atmospheric circulation over East Asia used in Part I, axis-orthogonal wind (U_{orth}, positive southwesterly) defined as the speed of the horizontal wind vector along orthogonal axis to the land-to-ocean line (130°E, 65°N–160°E, 35°N, Part I), shows negative (northeasterly) anomalies in 1 % CO$_2$ and amip4× CO$_2$ and a positive (southwesterly) anomaly in amipFuture (Fig. 4; Table 1).

The above results represent that the effects of CO$_2$ and SST play the distinct roles on the changes simulated in 1 % CO$_2$ run over the Far East. Previous studies (e.g. Lambert et al. 2011) revealed that the general characteristics of climate response to sum of the CO$_2$ and SST forcing can be largely simulated by the sum of the individual climate responses to the individual forcings although a nonlinearity term is not negligible. Now we examine the relationship of the responses simulated in the three experiments among the multi-models before we test an assumption of additivity of the CO$_2$ and SST forcings (see Sect. 4). Figure 6 shows relationship of the land–sea ΔSAT and $\Delta Z3085$ contrasts in the individual models. All the values are also listed in Table 1. The multi-model ensemble means in the individual simulations and their spreads reveal that: (1) the CO$_2$ and SST effects act as positive and negative contributions for the ΔSAT and $\Delta Z3085$ contrasts in the 1 % CO$_2$ run; and (2) inter-model variances show clear positive correlations between land–sea ΔSAT and $\Delta Z3085$ contrast in all the ensembles (correlation coefficients are 0.63, 0.74, and 0.58 in the 1 % CO$_2$, amip4× CO$_2$, and amipFuture, respectively). This means that the positive changes in the land–sea contrasts of the Far East in global warming experiment are determined by the large positive change due to CO$_2$ forcing and the small negative change due to SST increase.

It is also apparent that the responses in 1 % CO$_2$ runs are larger than the sum of the responses simulated in amip4× CO$_2$ and amipFuture. One factor is that the amplitude of global warming is generally larger in the amipFuture run than 1 % CO$_2$ run (multi-model means of ΔSAT_g are 3.91 and 4.55 K in 1 % CO$_2$ and amipFuture respectively, Table 1). The responses in amipFuture should be scaled by the ΔSAT_g ratio between amipFuture and 1 % CO$_2$ in the individual models when we compare the responses. Another factor for the discrepancy is a difference in spatial patterns of SST anomaly between 1 % CO$_2$ and amipFuture runs. The imposed SST anomaly in amipFuture shows anomalous warming in the mid-latitude western North Pacific and Sea of Okhotsk (e.g. Fig. 1 in Lu et al. 2008) but some models simulate weaker warming in that region in 1 % CO$_2$ run than the imposed SST. The difference of SST anomaly can influence the land–sea ΔSAT and tropospheric warming contrast over the Far East. For example, SST effects estimated by the responses in amipFuture run in some models including MPI-ESM-MR are overestimates (Table 1; Fig. 6) because those models simulate smaller warming in the western North Pacific in 1 % CO$_2$ run than the prescribed-SST. However, other models including MIROC5 simulate similar patterns of SST in 1 % CO$_2$ run to the prescribed-SST (see Sect. 4), resulting in better additivity of the CO$_2$ and SST effects than the other models (Table 1). We should note that this method has a limitation in decomposing the two effects quantitatively by using the results of AMIP-type sensitivity experiments conducted under the CMIP5 protocol. In the next section, we further examine the additivity of CO$_2$- and SST-induced influences on the projected changes in the transient warming experiments including RCP-type future scenario runs by using MIROC5 model.

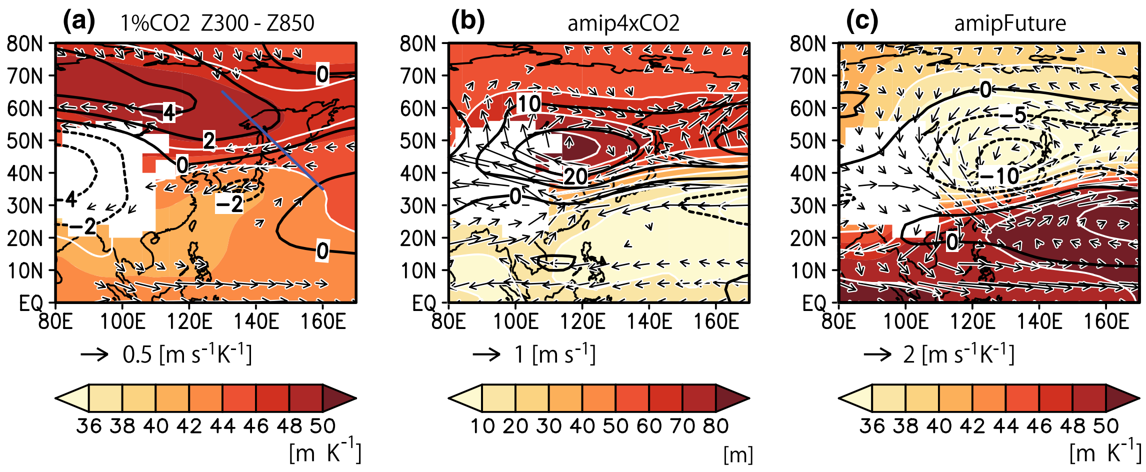

Fig. 4 Similar to Fig. 1a, b, d but for thickness between 300 and 850 hPa ($\Delta Z3085$, shade, m), horizontal wind anomaly at 850 hPa (m s^{-1}), and ΔZ_{eddy} at 300 hPa level ($\Delta Z_{eddy}300$, m) over the Far East and western North Pacific

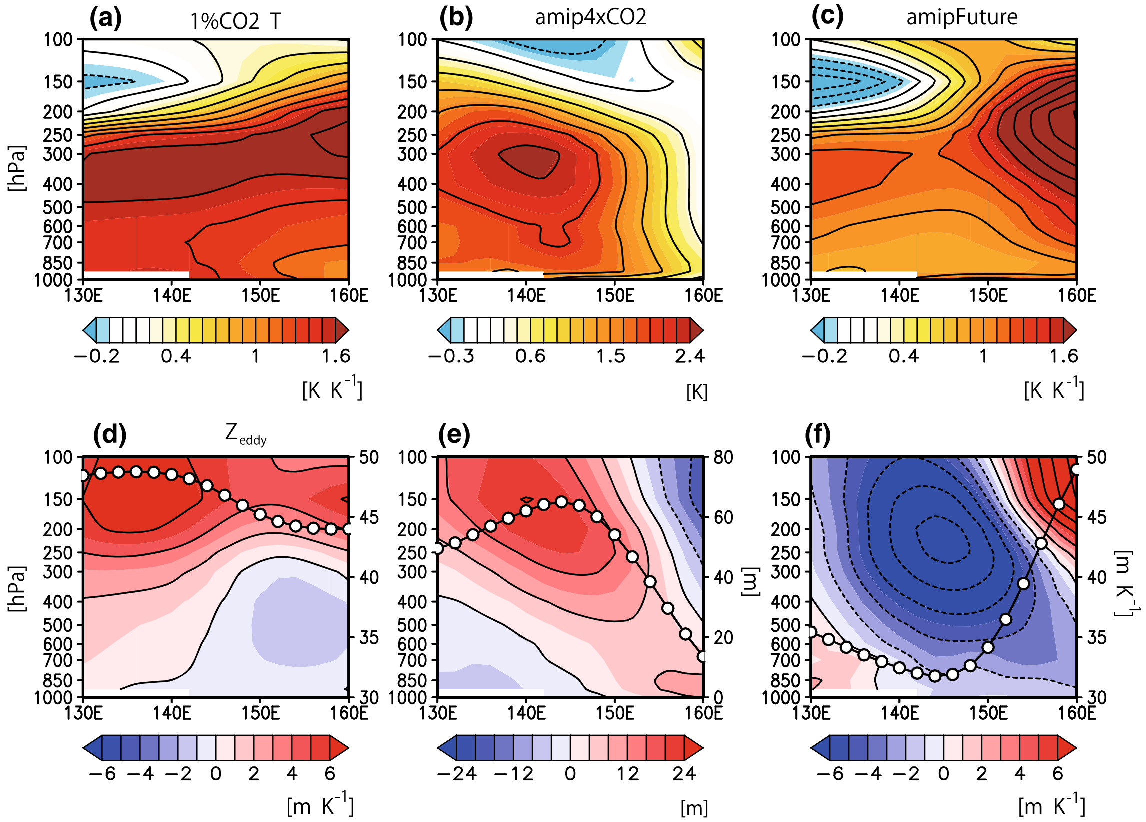

Fig. 5 Similar to Fig. 4 but for vertical structures of **a–c** ΔT and **d–f** difference of geopotential height on the land-to-ocean line (130°E, 65°N–160°E, 35°N, *blue line* in Fig. 4a). The *lines* in **d–f** represent $\Delta Z3085$ (m K^{-1} in **d**, **f**, m in **e**, *right axis*)

4 Decomposing effects of radiative forcing and surface temperature increase

It is suggested that the changes in land–sea contrast over the Far East in any runs of 1 % CO_2, RCPs, or the step experiment, could largely be decomposed into the positive effect of ΔF and the negative effect of other factors (e.g. SST increase). To confirm this hypothesis, we next investigate ΔF-dependent and other components of changes determined in the step experiment conducted with MIROC5 model. We also should take into account possible factors for errors in linearity (see Sect. 5).

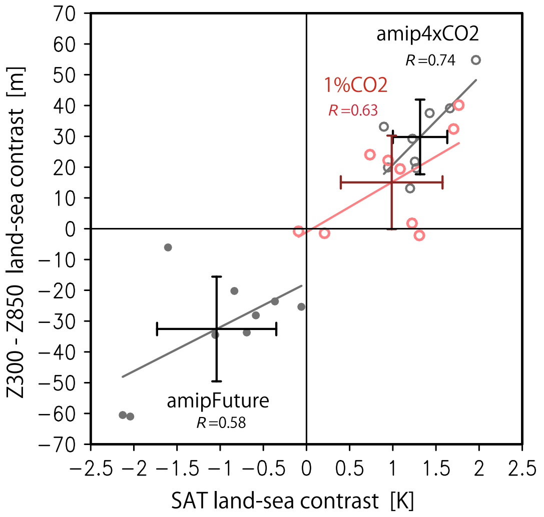

Fig. 6 A *scatter plot* of the land–sea ΔSAT (K) and $\Delta Z3085$ contrasts (m) in nine models of 1 % CO_2 (*red*), amip4× CO_2 (*open grey circle*), and amipFuture (*filled grey circle*). *Crosses* represent the nine models mean and the ranges of their ±1SDs. All the values are listed in Table 1. The *lines* represent least-square regressions. *R* means correlation coefficient

Figure 7a shows the change in the land–sea ΔSAT contrast over the Far East in the single-member step experiment (black crosses) and 12-member ensemble experiments (red crosses) starting from initial states 1 month apart to remove seasonality and increase the signal-to-noise ratio (Sect. 2.2 in Kamae and Watanabe 2013). The plot located near the y-axis ($\Delta SAT_g \approx 0$) means the effect of CO_2 forcing which is independent of ΔSAT_g. To quantify these effects, we utilize a regression method proposed in Gregory et al. (2004):

$$\Delta X \approx \Delta X_F + \alpha \Delta SAT_g, \qquad (3)$$

where ΔX is the change in a given variable in the step experiment, α is the slope of the regression line against ΔSAT_g, and ΔX_F is the y-axis intercept. ΔX_F and α at a given grid point determined by this method, represent the ΔF effect and ΔSAT_g effect, respectively. Note that the ΔF effect is equal to the CO_2 effect in any experiments with CO_2 forcing (1 % CO_2, step experiment, and amip4× CO_2) except the historical and those RCP runs including non-CO_2 forcings. This method has been adopted widely in studies on climate feedback, energy budgets, and the hydrological cycle in step experiments (e.g. Gregory and Webb 2008; Andrews et al. 2009; Bala et al. 2010; Watanabe et al. 2010; Kamae and Watanabe 2013).

The ΔF effect, represented by the fast response to CO_2 quadrupling, is consistent qualitatively (positive sign) and comparable quantitatively (2.06 K) with the CO_2 quadrupling as effect estimated by the amip4× CO_2 run (Table 1). This result indicates that the ΔF effect estimated by the AMIP-type simulation (amip4× CO_2) can largely reproduce the ΔF effect identified by the fast response to abrupt CO_2 increase in the CGCM run (abrupt4× CO_2). Although the ΔSAT contrast in the single-member run swings largely during the long-term integration because of the large interannual variability, the least-square regression lines in both of the two ensembles show clear declines of the ΔSAT contrast in response to the positive change in ΔSAT_g. The ΔSAT_g effect (-0.39 K K^{-1}) is determined by the slope of the regression line. Next, we attempt to reconstruct the results of the 1 % CO_2 run by the response in the step experiment, following Good et al. (2011, 2013) method detailed in Sect. 2.2. Figure 7b shows the ΔSAT contrast in the 1 % CO_2 run and its reconstruction by the step experiment. The reconstruction (blue curve) generally captures the 30-year running-mean of the 1 % CO_2 run (black curve). Note that the reconstruction skill is limited in the first 40 years because of weak forcing during this period. However, the values in the periods of CO_2 doubling (years 41–70) and quadrupling (years 111–140) are well reconstructed. In addition, the spatial pattern of ΔSAT in years 111–140, shown in Fig. 8a, is also well reconstructed by this method, indicating that the reconstruction skill is good when the forcing is sufficiently strong. Note that MIROC5 simulates the warming peak in the mid-latitude western North Pacific in 1 % CO_2 run (Fig. 8a) which is consistent with the prescribed-SST in amipFuture run (see Sect. 3.2).

According to the reconstruction, we decompose the reconstructed values in the 1 % CO_2 run into the ΔF effect (light blue) and ΔSAT_g effect (purple, Fig. 7b, c). The ΔF and ΔSAT_g effects contribute to the 1 % CO_2 run positively and negatively, and the former is larger than the latter both in the transient (Fig. 7b) and equilibrium state (Table 2), resulting in the positive sign in the reconstruction. The negative ΔU_{orth} in the 1 % CO_2 run is also attributed to the ΔF effect (Table 2). In principle, using this method, we can compare the ΔF and ΔSAT_g effects for any period in both the transient and equilibrium experiment; however, some potential problems might exist, which will be discussed in Sect. 5.

Figure 8 shows spatial patterns of the ΔF and ΔSAT_g effects on the reconstructed ΔSAT in the 1 % CO_2 run. They show positive and comparable contributions for positive ΔSAT over land in mid- and high-latitudes. The fraction of ΔF effects on the Far East ΔSAT is about 40 % over land (Fig. 8d) in contrast to the ΔSAT_g contribution on the ΔSAT over the ocean (Fig. 8c, e). Note that the relative contributions of the two are also comparable in the other seasons but the land–sea contrasts are relatively unclear than JJA (figure not shown). Further investigations would be needed to explain the spatial patterns of the contributions in the other seasons with particularly attention for influences of sea–ice reductions in the surrounding oceans.

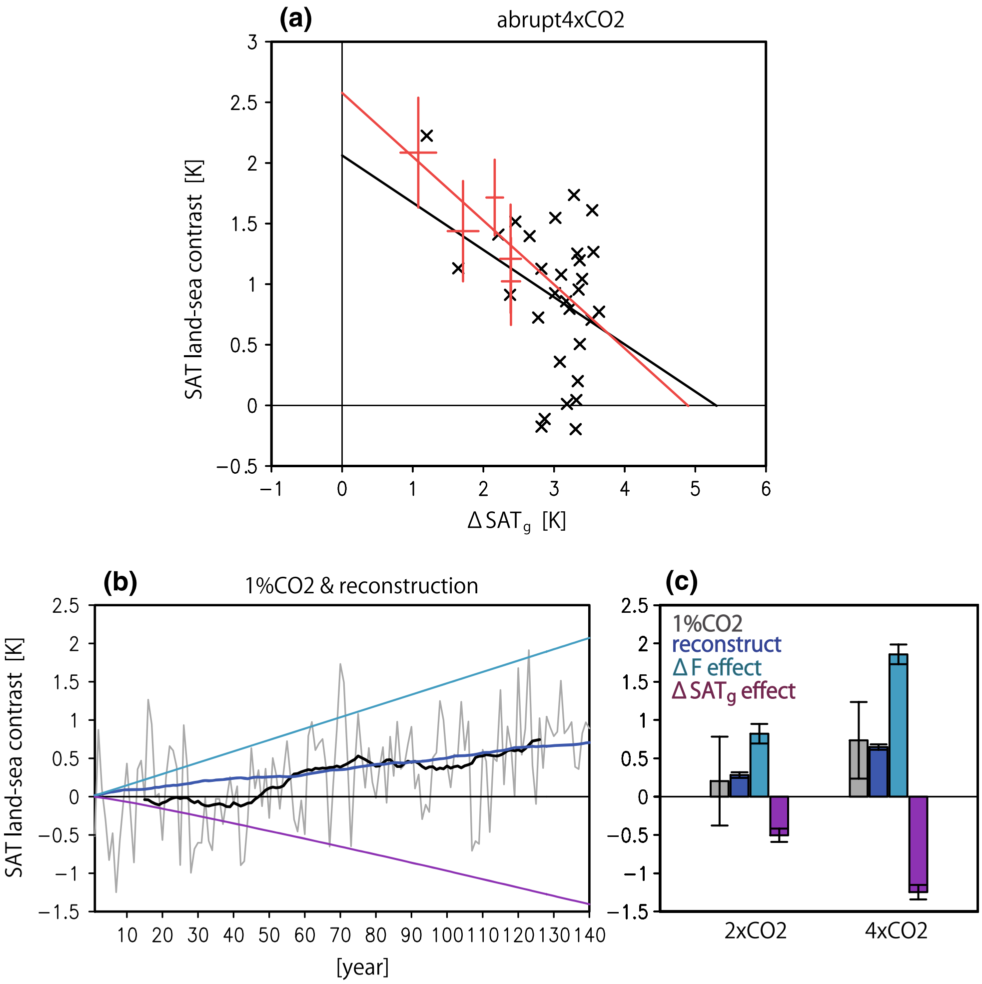

Fig. 7 MIROC5 step experiment and its application to reconstruction of the 1 % CO_2 run. **a** *Scatter plot* of the land–sea Δ*SAT* contrasts (K) in step experiment. *Black plots* represent a result of single member over 30 years. *Red crosses* are 12-member ensemble mean over 5 years and its ±1 SDs. The *lines* represent the least-square regressions. **b** Time series of Δ*SAT* land–sea contrast in 1 % CO_2 run (*gray*) and its 30-year running mean (*black*). *Blue curve* shows the reconstruction by the step experiment using the method detailed in Sect. 2.2. *Light blue* and *purple curves* are Δ*F* and ΔSAT_g effects on the reconstructed time series estimated by Eq. 2. **c** Comparison of four values averaged in year 41–70 (2× CO_2) and 111–140 (4× CO_2). *Error bars* are ±1 SDs of interannual variabilities in 30 years

Figure 9 shows the land- and ocean-mean Δ*SAT* during JJA over the Far East in relation to the annual-mean ΔSAT_g and Δ*F* in the individual experiments. Note that the transient changes shown in Fig. 9 (small circles) are the reconstructed 1 % CO_2 run (blue curve in Fig. 7b) which represent well the low-frequency variability in the 1 % CO_2 run (Fig. 7b, c). In the transient warming experiment (1 % CO_2 and RCP runs), both ΔSAT_g and Δ*F* increase gradually and the plotted marks shift to the upper right of the panels. In contrast, the plotted marks of the AMIP-type sensitivity experiments are located on the x-axis or near the y-axis because of fixed Δ*F* or Δ*SST* in these experiments (0 W m^{-2} and 0 K, respectively). The ΔSAT_g in the step experiment increases rapidly with constant Δ*F* owing to the CO_2 quadrupling (8.70 W m^{-2}). In the individual runs, the increase of the land-mean (ocean-mean) Δ*SAT* over the Far East region (color) follows largely the sum of the Δ*F* and ΔSAT_g effects (contour) obtained by the regression method using the results of the step experiment (Eq. 2). Namely, ΔX_F corresponds to the Δ*F* effect and $\alpha \Delta SAT_g$ represents the ΔSAT_g effect. We assume linearity and additivity of the forcings, which is discussed in Sect. 5. The land-mean Δ*SAT* increases in response to ΔSAT_g and Δ*F* result in the estimated contours being diagonally downwards to the right. In contrast, the estimated contour of the ocean-mean Δ*SAT* lies vertically because it is mostly determined by ΔSAT_g.

Figure 10 shows the land–sea Δ*SAT* contrast over the Far East in the individual runs with the ΔSAT_g and Δ*F*, i.e. the difference between Fig. 9a, b. The Δ*SAT* contrast shows negative and positive signs in response to increasing ΔSAT_g and Δ*F* respectively, resulting in the contour (sum of the two effects) being diagonally downwards to the left. The individual transient and sensitivity runs follow this relationship: the large positive change in amip4× CO_2 and the step experiments, the gradual increase in the 1 % CO_2 and RCP runs, and the large negative change in amipFuture. The signs of the transient runs are positive, according to the larger increase in the land-mean SAT compared with the ocean-mean (Fig. 9).

Figure 11 shows the Δ*Z3085* land–sea contrast over the Far East. It also shows similar features to those of the Δ*SAT*

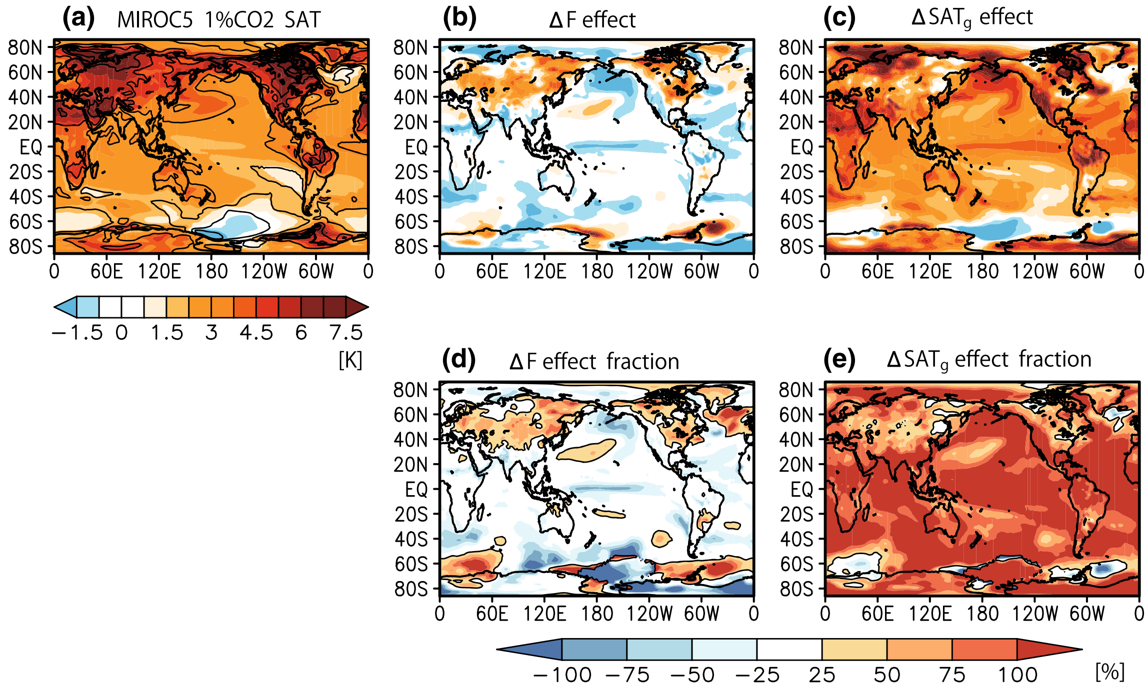

Fig. 8 Map of ΔF and ΔSAT_g effects on the reconstructed JJA-mean ΔSAT (K) in MIROC5 1 % CO_2 run. **a** Result of 1 % CO_2 run (*contour*, interval = 1.5 K) and its reconstruction (*shading*). **b** ΔF and **c** ΔSAT_g effects. **d** Fraction (%) of the ΔF and **e** ΔSAT_g effects on the reconstructed ΔSAT. *Contours* represent ±25 %

contrast (Fig. 10), indicating that both the ΔSAT and $\Delta Z3085$ contrasts over the Far East can be largely interpreted by the sum of the positive and negative effects of ΔF and ΔSAT_g. Note that some discrepancies between the sum of the two effects and the results of the runs are found. For example, the sign of change in SAT contrast in the 2041–2070 period of the RCP2.6 run is opposite to that estimated (Fig. 10). Some quantitative mismatches are also found in the ΔSAT and $\Delta Z3085$ land–sea contrasts (Figs. 10, 11), indicating some limitations and problems in the estimation method as discussed below.

5 Discussion

The opposing effects of ΔF and ΔSAT_g on the land–sea contrast over the Far East contribute positively and negatively to the projected change under global warming. The sum of these effects can reproduce the results of the simulations largely including the AMIP-type experiments (amip4× CO_2, amipFuture), transient warming experiments (1 % CO_2, RCP runs), and step experiment (abrupt4× CO_2, Figs. 9, 10, 11). Does a nonlinear term have any contributions on the results of those simulations? Lambert et al. (2011) revealed that no substantial nonlinearities were found in indices of atmospheric circulation and cloud radiative effect when the effects of ΔF associated with the doubling of CO_2 concentration and spatially uniform ΔSST were added to an AGCM. Deser and Phillips (2009) also revealed a high degree of linearity in the response to ΔF and ΔSST in atmospheric circulation trends during 1950–2000, simulated in an AGCM. As noted in Sect. 4, some inconsistencies are found between the linear summed estimation of the ΔF and ΔSAT_g effects on the land–sea contrast and the results of the simulations (Figs. 9, 10, 11). Possible factors contributing the discrepancies are discussed below.

One problem in the linear summed estimation method is the limited signal to noise ratio owing to the limited ensemble members and substantial interannual variability over the Far East (Fig. 7b, Part I). The limited signal to noise ratio may contribute to uncertainties in the estimated ΔF and ΔSAT_g effects particularly during the period when the imposed forcing and the response are weak (Fig. 7b, c). Another factor for the inconsistencies between the changes simulated in the individual runs (colors in Figs. 9, 10, 11) and the sum of the ΔF and ΔSAT_g effects (contours in Figs. 9, 10, 11) is the difference in the simulated spatial patterns of SST among the simulations. Although MIROC5 simulates similar SST pattern in 1 % CO_2 run generally to the prescribed SST in amipFuture (e.g. warming peak in the mid-latitude western North Pacific, Fig. 8a), some differences in regional SST anomalies can lead to a difference of land–sea warming contrasts over the Far East

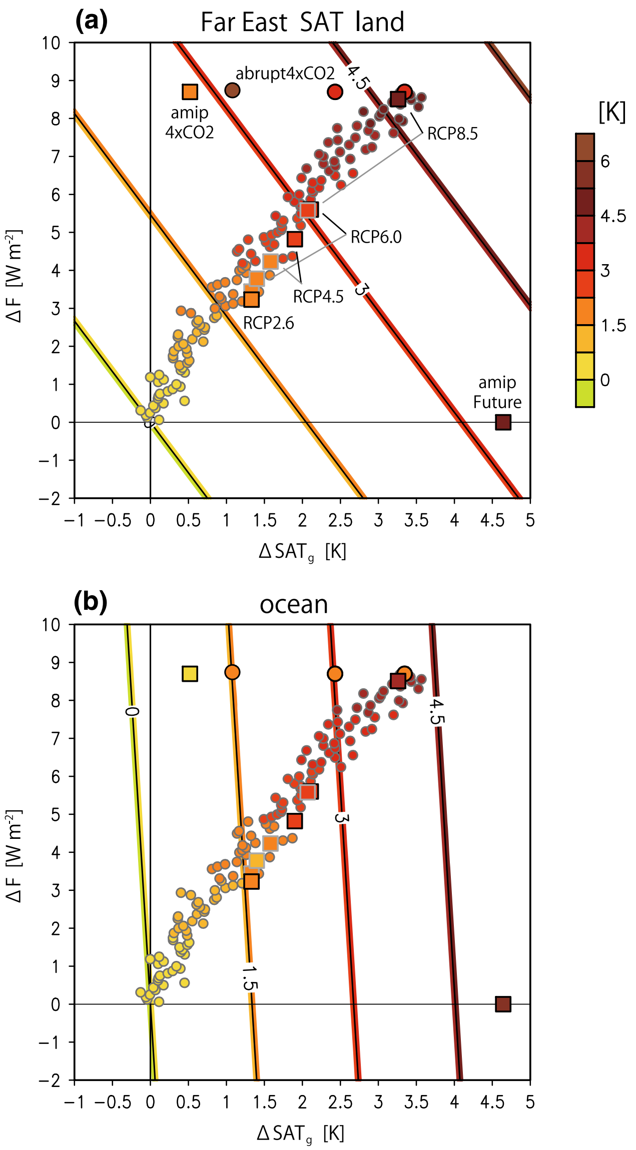

Fig. 9 Scatter diagram of ΔSAT_g and global-mean ΔF in the individual runs simulated in MIROC5. *Colors in plotting marks* are **a** land-mean, **b** ocean-mean ΔSAT over the Far East. *Sets of gray and black squares* are averages in the period 2041–2070 and 2071–2100 in RCP runs. *Three large circles* are the first year and 2–5 years mean in 12-member ensemble means, and 6–30 years mean in single-member, respectively (*left–right*). *Small circles* are the reconstructed 1 % CO_2 run (*blue curve* in Fig. 7b). The *isolines* represent **a** land-mean, **b** ocean-mean ΔSAT over the Far East estimated by the ΔF and ΔSAT_g effects (Eq. 3)

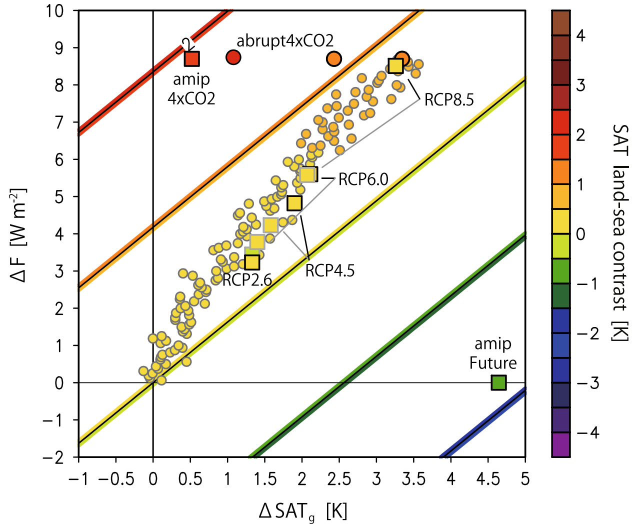

Fig. 10 Similar to Fig. 9 but for the land–sea ΔSAT contrast over the Far East (Table 2)

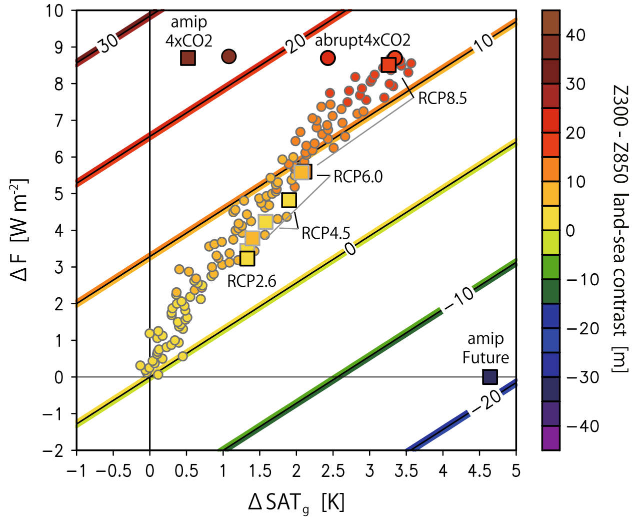

Fig. 11 Similar to Fig. 10 but for the $\Delta Z3085$ land–sea contrast over the Far East (Table 2)

between the simulations. In addition, differences of increasing SST simulated in the RCP runs with 1 % CO_2 run can also be factors for the inconsistencies. It is needed to examine how do these SST influence on responses of global and regional land–sea contrast in future works.

In Sect. 4, we apply the method reconstructing the transient responses from the step experiment. The reconstruction method of Good et al. (2013) applied to the RCP runs might not be valid when the non-CO_2 forcing is dominant in the given scenarios. The effects of regional non-CO_2 forcing, including aerosols in the RCP runs, on the land–sea contrast over the Far East cannot be reproduced by the method in this study. For example, differences of imposed forcing owing to changes of the atmospheric concentration of aerosols and land use might contribute to the regional ΔSAT, $\Delta Z3085$ and resultant changes of the land–sea contrast. In fact, some discrepancies are found, as detailed above. The possible influence of regional non-CO_2 forcing on the simulated change is another factor for the inconsistency between the changes simulated in the individual runs and the sum of the ΔF and ΔSAT_g effects.

The method assuming linear additivity by ΔF and ΔSAT_g effects used in this study has some problems described above. However, the reconstructions reproduce well the relationship that the run with stronger ΔF shows a larger change in land–sea contrast. The reconstruction has good skill in the scenarios with strong ΔF (i.e. 1 % CO_2 and RCP8.5) owing to the dominant effect of the much-increased ΔF due to increasing CO_2. We have to pay attention to the fact that this reconstruction cannot be applied when the non-CO_2 forcing has a relatively large contribution to the total change. We should also note that the different patterns of increasing SST simulated in given experiments can contribute to the simulated change in regional land–sea warming contrast substantially. We cannot apply this method to explain all the regional climate responses simulated in the transient warming experiments. However, we can conclude that the ΔF effect plays an important role in the land–sea contrast over the Far East during boreal summer in the projected future climate simulated in the CMIP5 models.

In this study, we tried to interpret the physical mechanism of the change in land–sea contrast over East Asia by decomposing ΔF and ΔSAT_g effects. The change of the land–sea contrast over East Asia can be largely explained by a part of the global characteristics that the relative importance of ΔF and ΔSAT_g effect depends on latitude (Figs. 1, 2, 8). However, the responses in the land–sea thermal contrast over mid- and high-latitude simulated in the SST experiments (amip4 K and amipFuture) show some regionalities (Fig. 1). The weaker warming of the free-troposphere relative to the surrounding regions is found over eastern and western sides of the Eurasian Continent. Further studies are needed to examine possible mechanisms and influences on projected regional climate change in the future scenario experiments.

The increase in summertime land–sea contrast over the Far East is not attributed to ΔSAT_g but CO_2-induced ΔF. This result suggests a possibility that the anomalous warming over land relative to the ocean in the mid- and high-latitude Northern Hemisphere could be used as an index of ΔF due to changes in atmospheric concentrations of greenhouse gases under given emission pathways. The changes in land–sea SAT contrast and associated atmospheric circulation in the future climate projections may be sensitive to given CO_2 concentration pathways including the cases of decreasing concentration (e.g. Cao et al. 2011). In addition, the kind of ΔF (CO_2 or solar radiation) in geoengineering method may affect the sign and magnitude of the changes. Bony et al. (2013) suggested that changes in dynamical component of tropical precipitation due to the direct effect of CO_2 increase may not be avoided by ΔSAT_g control with solar radiation management. The change in the land–sea contrast over the Far East gives another example of the importance of the direct effect by CO_2 increase. It is needed to assess effects of other types of forcings (anthropogenic aerosol emissions, volcanic eruptions, and solar radiation) and its additivity on changes of the thermodynamic structure and atmospheric circulation over the Far East in future works.

6 Conclusions

In this two-part paper, we examined the changes in the land–sea thermal contrast and summertime atmospheric circulation over East Asia under the global warming with observations and CMIP5 dataset. ΔSAT over land shows relatively larger increase in the recent decades than that over ocean, indicating the possible impact on the land–sea thickness contrast and associated atmospheric circulation pattern that accompanies a stronger northeasterly to northeastern Japan. The observed long-term changes of the land–sea SAT contrast in the recent decades are reproduced by CMIP5 multi-models, but with somewhat larger magnitude. The projected positive changes in land–sea SAT contrasts among the models are correlated with the change in the thickness contrast between them, indicating the positive changes in SAT and thickness contrasts are the part of the consistent responses to global warming among CMIP5 models.

The AMIP-type sensitivity experiments show positive and negative contributions of CO_2 quadrupling and SST increase to the projected future change in land–sea contrast over the Far East. The projected positive ΔSST contributes to strengthen the SAT contrast in low latitudes but not in the mid- and high-latitude because of limited warming in the free troposphere over the interior of the continent. The transient changes of land–sea contrast in 1 % CO_2 and RCP experiments can be approximated by the sum of the positive effect of global ΔF due to CO_2 increase and negative effect of ΔSAT_g. The experiment with larger ΔF shows larger increase in land–sea contrast than that with the smaller ΔF experiment due to the larger effect summed of the two (ΔF and ΔSAT_g effects) over land relative to ocean.

This study gives an example that the direct effect of CO_2 increase is essential for the regional climate change projected in the future scenario experiments. Bony et al. (2013) also pointed its importance on the projected change in the dynamical tropical precipitation. The distinct influences of the increases in atmospheric CO_2 and SST have mainly been focused on the changes of the mean climate states. In future studies, respective roles of the imposed forcings on climate variability and frequency of extreme events should be examined to assess possible risks to ecosystems and society associated with severe climate events due to the different climate forcings.

Acknowledgments We acknowledge the World Climate Research Programme's Working Group on Coupled Modeling, which is responsible for CMIP, and we thank the climate modeling groups (listed in Table 1) for producing and making available their model output. For CMIP5, the US Department of Energy's Program for Climate Model Diagnosis and Intercomparison provided coordinating support, and led development of software infrastructure in partnership with the Global Organization for Earth System Science Portals. We would like to acknowledge Tokuta Yokohata, Tomoo Ogura and Seita Emori for providing helpful comments and suggestions. The authors are grateful to two anonymous reviewers for their constructive comments. This work was supported by the Program for Risk Information on Climate Change (SOUSEI program) from the Ministry of Education, Culture, Sports, Science and Technology (MEXT), Japan.

References

Allen MR, Ingram WJ (2002) Constraints on future changes in climate and the hydrologic cycle. Nature 419:224–232

Andrews T, Forster PM, Gregory JM (2009) A surface energy perspective on climate change. J Clim 22:2557–2570

Arai M, Kimoto M (2008) Simulated interannual variation in summertime atmospheric circulation associated with the East Asian monsoon. Clim Dyn 31:435–447

Bala G, Caldeira K, Nemani R (2010) Fast versus slow response in climate change: implications for the global hydrological cycle. Clim Dyn 35:423–434

Bayr T, Dommenget D (2013) The troposphere land–sea warming contrast as the driver of tropical sea level pressure changes. J Clim 26:1387–1402

Boer GJ (2011) The ratio of land to ocean temperature change under global warming. Clim Dyn 37:2253–2270

Bony S, Webb MJ, Bretherton CS, Klein SA, Siebesma AP, Tselioudis G, Zhang M (2011) CFMIP: towards a better evaluation and understanding of clouds and cloud feedbacks in CMIP5 models. CLIVAR Exch 16(56):20–24

Bony S, Bellon G, Klocke D, Sherwood S, Fermepin S, Denvil S (2013) Robust direct effect of carbon dioxide on tropical circulation and regional precipitation. Nat Geosci 6:447–451

Bracco A, Kucharski F, Kallummal R, Molteni F (2004) Internal variability, external forcing and climate trends in multi-decadal AGCM ensembles. Clim Dyn 23:659–678

Cao L, Bala G, Caldeira K (2011) Why is there a short-term increase in global precipitation in response to diminished CO_2 forcing? Geophys Res Lett 38:L06703. doi:10.1029/2011GL046713

Cao L, Bala G, Caldeira K (2012) Climate response to changes in atmospheric carbon dioxide and solar irradiance on the time scale of days to weeks. Environ Res Lett 7:034015

Chadwick R, Good P, Andrews T, Martin G (2014) Surface warming patterns drive tropical rainfall pattern responses to CO_2 forcing on all timescales. Geophys Res Lett 41:610–615. doi:10.1002/2013GL058504

Collins M et al (2010) The impact of global warming on the tropical Pacific Ocean and El Niño. Nat Geosci 3:391–397

Compo GP, Sardeshmukh PD (2009) Oceanic influences on recent continental warming. Clim Dyn 32:333–342

Demoto S, Watanabe M, Kamae Y (2013) Mechanism of tropical low-cloud response to surface warming using weather and climate simulations. Geophys Res Lett 40:2427–2432. doi:10.1002/grl.50474

Deser C, Phillips AS (2009) Atmospheric circulation trends, 1950–2000: the relative roles of sea surface temperature forcing and direct atmospheric radiative forcing. J Clim 22:396–413

Dommenget D (2009) The ocean's role in continental climate variability and change. J Clim 22:4939–4952

Dong B, Gregory JM, Sutton RT (2009) Understanding land–sea warming contrast in response to increasing greenhouse gases. Part I: transient adjustment. J Clim 22:3079–3097

Doutriaux-Boucher M, Webb MJ, Gregory JM, Boucher O (2009) Carbon dioxide induced stomatal closure increases radiative forcing via a rapid reduction in low cloud. Geophys Res Lett 36:L02703. doi:10.1029/2008GL036273

Fasullo J (2012) A mechanism for land–ocean contrasts in global monsoon trends in a warming climate. Clim Dyn 39:1137–1147

Folland CK, Sexton DMH, Karoly D, Johnson C, Rowell D, Parker D (1998) Influences of anthropogenic and oceanic forcing on recent climate change. Geophys Res Lett 25:353–356

Forster PMD, Taylor KE (2006) Climate forcings and climate sensitivities diagnosed from coupled climate model integrations. J Clim 19(23):6181–6194

Good P, Gregory JM, Lowe JA (2011) A step-response simple climate model to reconstruct and interpret AOGCM projections. Geophys Res Lett 38:L01703. doi:10.1029/2010GL045208

Good P, Gregory JM, Lowe JA, Andrews T (2013) Abrupt CO_2 experiments as tools for predicting and understanding CMIP5 representative concentration pathway projections. Clim Dyn 40:1041–1053

Gregory JM, Webb MJ (2008) Tropospheric adjustment induces a cloud component in CO_2 forcing. J Clim 21:58–71

Gregory JM et al (2004) A new method for diagnosing radiative forcing and climate sensitivity. Geophys Res Lett 31:L03205. doi:10.1029/2003gl018747

Huang P, Xie S-P, Hu K, Huang G, Huang R (2013) Patterns of the seasonal response of tropical rainfall to global warming. Nat Geosci 6:357–361

Jones GS, Stott PA, Christidis N (2013) Attribution of observed historical near surface temperature variations to anthropogenic and natural causes using CMIP5 simulations. J Geophys Res Atmos 118:4001–4024. doi:10.1002/jgrd.50239

Joshi MM, Gregory JM, Webb MJ, Sexton DMH, Johns TC (2008) Mechanisms for the land–sea warming contrast exhibited by simulations of climate change. Clim Dyn 30:455–465

Joshi MM, Lambert FH, Webb MJ (2013) An explanation for the difference between twentieth and twenty-first century land–sea warming ratio in climate models. Clim Dyn 41:1853–1869

Kamae Y, Watanabe M (2012) On the robustness of tropospheric adjustment in CMIP5 models. Geophys Res Lett 39:L23808. doi:10.1029/2012GL054275

Kamae Y, Watanabe M (2013) Tropospheric adjustment to increasing CO_2: its timescale and the role of land–sea contrast. Clim Dyn 41:3007–3024

Kamae Y, Watanabe M, Kimoto M, Shiogama H (2014) Summertime land–sea thermal contrast and atmospheric circulation over East Asia in a warming climate—Part I: Past changes and future projections. Clim Dyn. doi:10.1007/s00382-014-2073-0

Kimoto M (2005) Simulated change of the East Asian circulation under the global warming scenario. Geophys Res Lett 32:L16701. doi:10.1029/2005GL023383

Lambert FH, Chiang JCH (2007) Control of land–ocean temperature contrast by ocean heat uptake. Geophys Res Lett 34:L13704. doi:10.1029/2007GL029755

Lambert FH, Webb MJ, Joshi MM (2011) The relationship between land–ocean surface temperature contrast and radiative forcing. J Clim 24:3239–3256

Li W, Li L, Ting M, Liu Y (2012) Intensification of Northern Hemisphere subtropical highs in a warming climate. Nat Geosci 5:830–834

Lu J, Chen G, Frierson DMW (2008) Response of the zonal mean atmospheric circulation to El Niño versus global warming. J Clim 21:5835–5851

Ma J, Xie S-P (2013) Regional patterns of sea surface temperature change: a source of uncertainty in future projections of precipitation and atmospheric circulation. J Clim 26:2482–2501

Manabe S, Stouffer RJ, Spelman MJ, Bryan K (1991) Transient responses of a coupled ocean-atmosphere model to gradual changes of atmospheric CO_2. Part I: annual mean response. J Clim 4:785–818

Meinshausen M et al (2011) The RCP greenhouse gas concentrations and their extensions from 1765 to 2300. Clim Chang 109:213–241

Mitchell JFB, Wilson CA, Cunnington WM (1987) On CO2 climate sensitivity and model dependence of results. Q J R Meteorol Soc 113:293–322

Serreze MC, Barry RG (2011) Processes and impacts of Arctic amplification: a research synthesis. Glob Planet Chang 77:85–96

Sobel AH, Nilsson J, Polvani LM (2001) The weak temperature gradient approximation and balanced tropical moisture waves. J Atmos Sci 58:3650–3665

Sun Y, Ding Y, Dai A (2010) Changing links between South Asian summer monsoon circulation and tropospheric land-sea thermal contrasts under a warming scenario. Geophys Res Lett 37:L02704. doi:10.1029/2009GL041662

Sutton RT, Dong B, Gregory JM (2007) Land–sea warming ratio in response to climate change: IPCC AR4 model results and comparison with observations. Geophys Res Lett 34:L02701. doi:10.1029/2006GL028164

Taylor KE, Stouffer RJ, Meehl GA (2012) An overview of CMIP5 and the experiment design. Bull Am Meteorol Soc 90:485–498

Tomassini L et al (2013) The respective roles of surface temperature driven feedbacks and tropospheric adjustment to CO_2 in CMIP5 transient climate simulations. Clim Dyn 41:3103–3126

Ueda H, Iwai A, Kuwako K, Hori ME (2006) Impact of anthropogenic forcing on the Asian summer monsoon as simulated by eight GCMs. Geophys Res Lett 33:L06703. doi:10.1029/2005GL025336

Watanabe M et al (2010) Improved climate simulation by MIROC5: mean states, variability, and climate sensitivity. J Clim 23:6312–6335

Webb MJ, Lock AP (2013) Coupling between subtropical cloud feedback and the local hydrological cycle in a climate model. Clim Dyn 41:1923–1939

Widlandky MJ et al (2013) Changes in South Pacific rainfall bands in a warming climate. Nat Clim Chang 3:417–423

Wu G, Liu Y, He B, Bao Q, Duan A, Jin F-F (2012) Thermal controls on the Asian summer monsoon. Sci Rep 2:404. doi:10.1038/srep00404

Zhu C, Wang B, Qian W, Zhang B (2012) Recent weakening of northern East Asian summer monsoon: a possible response to global warming. Geophys Res Lett 39:L09701. doi:10.1029/2012GL051155